



Graphene-modified nanosized Ag_3PO_4 photocatalysts for enhanced visible-light photocatalytic activity and stability

Quanjun Xiang*, Di Lang, Tingting Shen, Fan Liu

College of Resources and Environment, Huazhong Agricultural University, Wuhan 430070, PR China

ARTICLE INFO

Article history:

Received 14 April 2014

Received in revised form 23 June 2014

Accepted 26 June 2014

Available online 5 July 2014

Keywords:

Nanosized Ag_3PO_4

Graphene

Photocatalytic activity

Stability

Synergetic effects

ABSTRACT

Novel Ag_3PO_4 photocatalyst possesses high visible-light photocatalytic activity, but the large crystallite size and the photocorrosion severely limit its practical application. It is highly desirable to develop new Ag_3PO_4 photocatalytic systems with nanosized structure and good photocatalytic stability. In this work, we prepare new graphene-modified nanosized Ag_3PO_4 photocatalyst by *in situ* growth strategy in an organic solvent. The as-prepared nanosized Ag_3PO_4 particles–graphene composite exhibits enhanced visible-light photocatalytic activity and stability toward the degradation of methylene blue (MB) in aqueous solution compared with bare nanosized Ag_3PO_4 particles and conventional large-sized Ag_3PO_4 particles–graphene composite. This enhanced photocatalytic activity and stability arise from the positive synergetic effects of the nanosized Ag_3PO_4 particles and graphene sheets including an increase in the number of active adsorption sites, suppression of charge recombination, reducing the formation of Ag nanoparticles. This work shows a great potential of nanosized Ag_3PO_4 particles–graphene composite for environmental purification of organic pollutants.

© 2014 Elsevier B.V. All rights reserved.

1. Introduction

In the past decades, there has been a great interest in developing semiconductor photocatalysts with high catalytic efficiency and good stability for water splitting and removal of hazardous organic compounds in industrial wastewater [1–5]. To date, various metal oxides, sulfide, silver halides, and their derivatives photocatalysts have been developed for the aforementioned purpose [1–12]. However, the development of high-efficiency visible-light-driven photocatalysts still remains a challenge. Recently, Ye et al. reported that a silver orthophosphate semiconductor photocatalyst (Ag_3PO_4) showed a good photocatalytic performance for oxygen production by water splitting and for the degradation of organic pollutants in aqueous solution under visible-light irradiation [13,14]. This novel photocatalyst exhibited a quantum efficiency of up to 90% for O_2 evolution from water splitting at wavelengths longer than 420 nm, which is significantly higher than that of other semiconductors reported in the literature [2–4]. However, Ag_3PO_4 is unstable under prolonged light illumination due to the photocorrosion by the photogenerated electrons, and its practical application is greatly limited. To resolve this problem,

diverse techniques have been proposed to improve the stability of Ag_3PO_4 , for example, by designing a core–shell nanostructure, coupling Ag_3PO_4 with metals as plasmonic structures, and forming complexes with heterostructures, etc [15–24]. Very recently, there is an increasing interest in combining Ag_3PO_4 with graphene or reduced graphene oxide to improve its stability and catalytic performance [22–24].

In recent years, graphene or graphene oxide (GO) has attracted tremendous attention due to its large surface area and high carrier mobility. Graphene has been demonstrated to be a promising candidate for the fabrication of various graphene-based composite photocatalysts [4–6,22–29]. Up to now, various graphene-based photocatalysts, for example, GO/ TiO_2 [25], graphene–CdS [26], GO/ ZnO [27,28] and GO/Ag/AgX (X = Cl, Br) [29] have been reported, and these composites show significantly enhanced photocatalytic activity due to the improved interfacial contact and enhanced adsorption activity of graphene or GO in these systems. In particular, the introduction of graphene sheets into Ag_3PO_4 could not only enhance the photocatalytic performance for the degradation of pollutants, but also significantly improve the stabilities of Ag_3PO_4 . Liu et al. reported the GO– Ag_3PO_4 composite synthesized through an ion-exchange method and showed their improved antibacterial activity toward *Escherich coli* and the enhanced photocatalytic activity for degradation of organic pollutants and stability [22]. Yang et al. developed a hydrothermal method to produce

* Corresponding author.

E-mail address: xiangqj@mail.hzau.edu.cn (Q. Xiang).

Ag₃PO₄–graphene composite photocatalysts with improved the photocatalytic performance and stability [24]. However, the particles sizes of Ag₃PO₄ in the above Ag₃PO₄–graphene composite is relatively large (0.5–2 μm), which intrinsically limits the photocatalytic activity due to the relatively large particle size and thus small specific surface area. Clearly, it is highly desirable to develop nanosized Ag₃PO₄ particles–graphene composites instead of large-sized Ag₃PO₄ particles.

In this study, a novel nanosized Ag₃PO₄ particles–graphene composite photocatalyst was prepared by *in situ* growth strategy in an organic solvent. The obtained nanosized Ag₃PO₄ particles–graphene composite exhibits enhanced visible-light photocatalytic activity and stability toward the degradation of MB in aqueous solution compared with bare nanosized Ag₃PO₄ particles. This novel composite also shows higher photocatalytic activity than that reported for conventional large-sized Ag₃PO₄ particles–graphene composites. Moreover, the photocorrosion of Ag₃PO₄ and the mechanisms of the enhanced photocatalytic performance for the graphene-modified Ag₃PO₄ composite were studied and discussed.

2. Experimental

2.1. Sample preparation

All the reagents were reagent-grade and deionized water was used in the whole experiment. Graphene oxide (GO) sheets were synthesized from natural graphite powders by a modified Hummers' method [30]. Nanosized Ag₃PO₄ particles–graphene (NAG) composite was prepared by *in situ* growth strategy in an organic solvent. First, 1.7 g of silver nitrate and 8.2 mL of oleylamine were dissolved in 30 mL of toluene. 4 mg of the prepared GO was dispersed in a solution of ethanol (10 mL) by ultrasonic treatment for 2 h, and then 0.67 mL of phosphoric acid solution (85 wt.%) was added to the obtained GO solution under magnetic stirring. Then, the above mixed solutions of GO and phosphoric acid was gradually added to the obtained toluene solution of silver nitrate and oleylamine under stirring. After 1 h of stirring, excess ethanol was added to precipitate Ag₃PO₄–GO composite. Then, the obtained precipitates were then re-dispersed in toluene and re-precipitated in ethanol for three times to remove all unreacted reagents. The resulting toluene solution of Ag₃PO₄–GO composite were irradiated with a 350 W Xe arc lamp for 15 min to reduce GO. In order to remove oleylamine surfactant, the as-prepared nanosized Ag₃PO₄–graphene composite was treated with dilute NH₄OH solution. For comparison, the bare nanosized Ag₃PO₄ particles (NA) without graphene sheets were also prepared under the same experimental condition. In addition, conventional large-sized Ag₃PO₄ particles–graphene (LAG) composites and bare large-sized Ag₃PO₄ particles (LA) were prepared by a precipitation method according to the procedures reported elsewhere [22]. The N-doped TiO₂ (N-TiO₂) was also prepared for reference by a sol–gel and calcination method [31].

2.2. Characterization

Powder X-ray diffraction (XRD) patterns were obtained on a Bruker D8 Advance diffractometer with Ni-filtered Cu Kα radiation (λ = 0.15418 nm) at a scan rate (2θ) of 0.05° s^{−1}. The accelerating voltage and the applied current were 40 kV and 40 mA, respectively. Scanning electron microscopy (SEM) was performed using a S-4800 microscope (Hitachi, Japan). Transmission electron microscopy (TEM) was conducted on a Tecnai G² F20 S-TWIN microscope at an accelerating voltage of 200 kV. The Brunauer–Emmett–Teller specific surface areas (S_{BET}) and porosity of the samples were

evaluated on the basis of nitrogen adsorption isotherms measured at −196 °C using an Autosorb-1 standard physical adsorption analyzer (Quantachrome Autosorb-1). All the samples were degassed at 110 °C before nitrogen adsorption measurements. The BET surface area was determined using adsorption data in the relative pressure (P/P₀) range of 0.05–0.3. The desorption data were used to determine the pore size distribution via the Barret–Joyner–Halender (BJH) method [32]. UV–vis absorbance spectra were obtained for the dry-pressed disk samples with a Perkin–Elmer Lambda 750 UV/vis spectrophotometer. Raman spectra were recorded at room temperature using a micro-Raman spectrometer (Renishaw InVia) in the backscattering geometry with a 514.5 nm Ar⁺ laser as an excitation source. The Fourier transform infrared spectra (FTIR) of the samples were recorded using an IRAffinity-1 FTIR spectrometer. X-ray photoelectron spectroscopy (XPS) measurements were performed by using an ultrahigh vacuum VG ESCALAB 210 electron spectrometer equipped with a multichannel detector. The spectra were excited using Mg Kα (1253.6 eV) radiation (operated at 200 W) of a twin anode in the constant analyzer energy mode with a pass energy of 30 eV. Photoluminescence (PL) spectra were obtained by using a Fluorescence Spectrophotometer (F-7000, Hitachi, Japan) at room temperature, and the wavelength of excitation was 315 nm.

2.3. Photocatalytic activity

The photocatalytic activity of the prepared samples for the photocatalytic oxidation (PCO) of methylene blue (MB) aqueous solution was measured under visible-light illumination at ambient temperature, as reported in the previous studies [33]. Experiments were as follows: 0.05 g of the sample was dispersed in 20 mL of an aqueous solution of MB (2 × 10^{−5} M). Prior to irradiation, the suspensions were stirred in the dark condition for 1 h to reach an adsorption–desorption equilibrium. A 350 W Xe arc lamp which equipped with an UV-cutoff filter (≤420 nm) was used as a visible-light source (35 cm far away from the photocatalytic reactor). The powders were then separated by centrifugation, and the concentration of MB was determined by measuring the absorbance peak at 664 nm using UV–vis spectrophotometer. Hydroxyl radicals (•OH) on the surface of the visible-light-illuminated NAG sample was detected by a photoluminescence (PL) method using terephthalic acid as a probe molecule [34]. Experimental procedure was similar to the measurement of photocatalytic activity except that the MB aqueous solution was replaced by the 5 × 10^{−4} M terephthalic acid aqueous solution with a concentration of 2 × 10^{−3} M NaOH.

3. Results and discussion

3.1. Characterization of as-prepared samples

Nanosized Ag₃PO₄ particles–graphene (NAG) composite and nanosized Ag₃PO₄ particles (NA) were prepared by *in situ* growth strategy in an organic solvent, and conventional large-sized Ag₃PO₄ particles–graphene (LAG) composite and bare large-sized Ag₃PO₄ particles (LA) were prepared by a precipitation method in aqueous solution. XRD patterns of the all as-prepared samples were indexed to the body-centered cubic structure of Ag₃PO₄ (JCPDS No. 06-0505) (see Fig. 1). For the NAG and LAG composites, no characteristic diffraction peaks for graphene and GO were observed in the patterns due to the low amount and/or the low diffraction intensity. It should be noted that the XRD peak intensities of the NA and NAG samples is weaker than that of the LA and LAG samples, indicated that Ag₃PO₄ particles in NA and NAG samples have smaller crystallite size compared with that in LA and LAG. The electron microscopy images further support this above result. Fig. 2a shows a typical

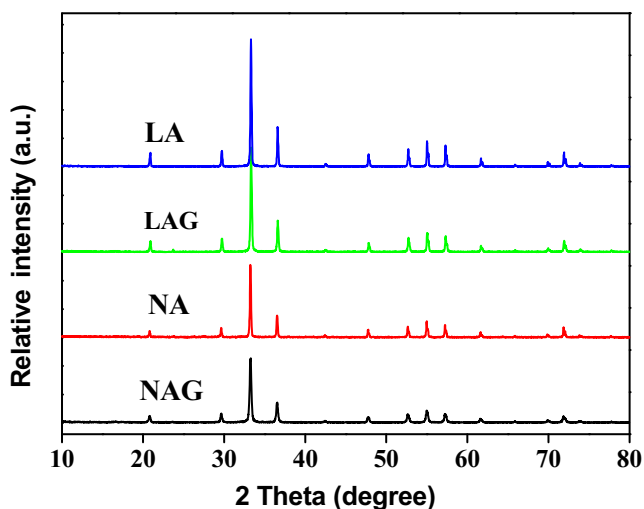


Fig. 1. XRD patterns of the LA, LAG, NA and NAG samples.

SEM image of the LA sample. As can be seen from this figure, bare Ag_3PO_4 particles possess irregular particle morphology with diameters of 0.5–1.5 μm , which is consistent with the results reported by Yi et al. [13]. The SEM image of the LAG sample was shown in Fig. 2b. Some Ag_3PO_4 particles were distinctly enwrapped with wrinkle-like graphene sheets, and the morphology and size of the Ag_3PO_4 in LAG sample is similar with that of bare Ag_3PO_4 . Fig. 2c shows a TEM image of the NAG sample prepared in an organic solvent. It can be seen that the nanosized Ag_3PO_4 particles are dispersed on

the surfaces of graphene sheets in the NAG sample, and the average size of Ag_3PO_4 nanoparticles is in the range of 20–50 nm, which is much smaller than that of the Ag_3PO_4 particles in LA and LAG samples as mentioned above. The corresponding high-magnification TEM image (Fig. 2d) of the Ag_3PO_4 nanocrystal shows clearly the crystalline lattice fringes. The angle between the crossing lattice fringes is 66° , and the lattice spacing are 0.268 and 0.239 nm, corresponding to the (2 1 0) and (2 1 1) planes of cubic Ag_3PO_4 phase, respectively [13,14].

The BET specific surface areas and porous structure of the Ag_3PO_4 samples are investigated by nitrogen sorption analysis. Fig. 3 shows the nitrogen sorption isotherms and the corresponding pore size distribution curves (inset in Fig. 3) for the LAG and NAG samples. The isotherms of the two samples are similar and displayed a type IV shape with a narrow hysteresis loop, indicating the existence of slit-like pores associated with the aggregation of graphene sheets [32,35]. However, the aforementioned two samples give a different BET specific surface area value due to the different particle size. The specific surface area of the NAG sample ($18.7\text{ m}^2\text{ g}^{-1}$) is much higher than that of the LAG sample ($0.8\text{ m}^2\text{ g}^{-1}$). Such high surface-to-volume for NAG might be extremely useful in photocatalytic process as they would provide more active sites for adsorption of reactant molecules.

The UV–vis diffuse reflectance spectra of the prepared samples (NA, NAG, LA and LAG) are shown in Fig. 4. Bare Ag_3PO_4 (NA and LA) samples show a strong absorption with absorption edge at about 530 nm, associated with the intrinsic band gap absorption of Ag_3PO_4 . With the introduction of graphene, Ag_3PO_4 –graphene composites (samples NAG and LAG) display a broad background absorption in the range of 550–800 nm. This can be attributed to

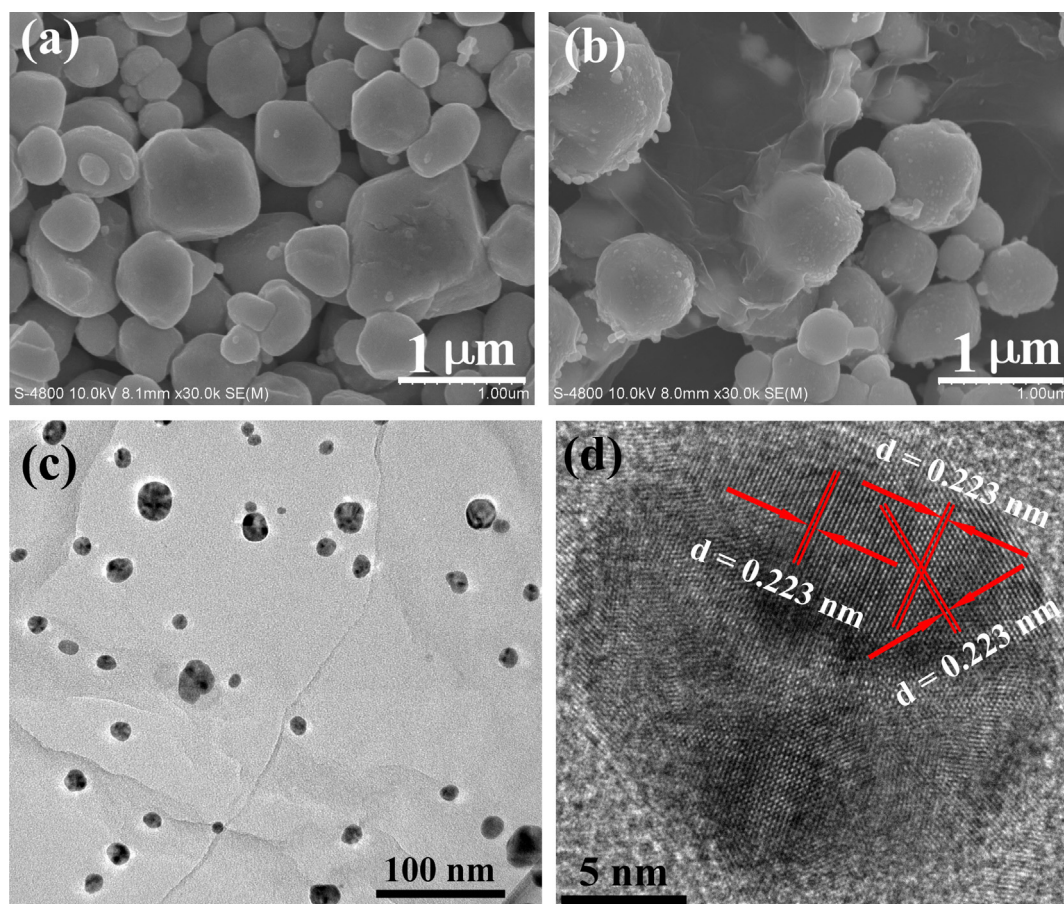


Fig. 2. SEM ((a) and (b)), TEM (c) and HRTEM (d) images of the LA (a), LAG (b) and NAG ((c) and (d)) samples.

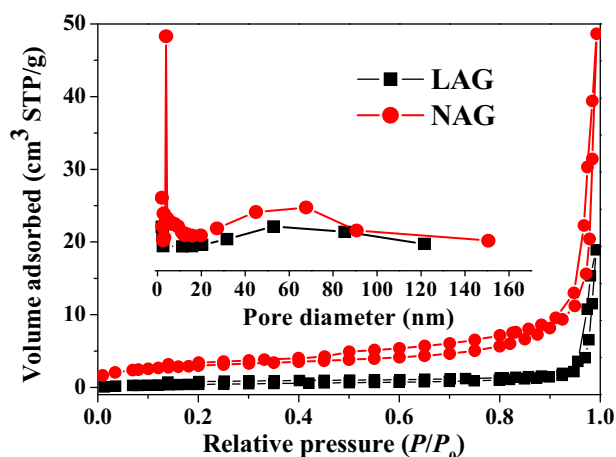


Fig. 3. Nitrogen sorption isotherms and the corresponding pore size distribution curves (inset) of the LAG and NAG samples.

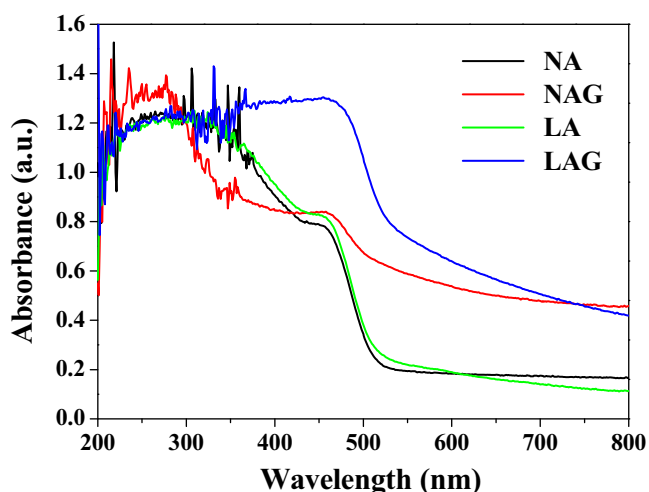


Fig. 4. UV–vis diffuse reflection spectra of the LA, LAG, NA and NAG samples.

the presence of graphene in the composite samples. Also, the LAG sample shows the enhanced absorption at about 500 nm compared with the NAG and pure Ag_3PO_4 sample, which is attributed to the higher content of graphene on the surface of the LAG sample and then results in dark gray of color. A further observation indicates that the absorption edges of the aforementioned composite samples are not shifted as compared with that of bare Ag_3PO_4 samples, indicating that carbon was not incorporated to the lattice of Ag_3PO_4 .

The Raman and Fourier transform infrared (FTIR) spectra are used to further characterize Ag_3PO_4 and graphene in the Ag_3PO_4 -graphene composites. Fig. 5a shows the Raman spectra of GO, bare Ag_3PO_4 (sample NA), and Ag_3PO_4 -graphene composite (sample NAG). The two prominent peaks at 1355 cm^{-1} and 1595 cm^{-1} are observed in the Raman spectrum of GO, corresponding to the well-documented D and G bands, respectively [11]. In the Raman spectrum of bare Ag_3PO_4 , there are several characteristic peaks at 550, 710, 905 and 990 cm^{-1} , which is consistent with the previous report [24]. For the Ag_3PO_4 -graphene composite, all the Raman bands for Ag_3PO_4 and the two characteristic peaks for the graphitized structures can be observed in the Raman spectroscopy of Ag_3PO_4 -graphene composite. Fig. 5b shows the FTIR spectra of GO, bare Ag_3PO_4 and Ag_3PO_4 -graphene composite. In case of GO, four characteristic absorption peaks in the $1000\text{--}1800\text{ cm}^{-1}$ region are observed. The two peaks at 1064 and 1391 cm^{-1} correspond to the C–O stretching vibrations and tertiary C–OH groups stretching,

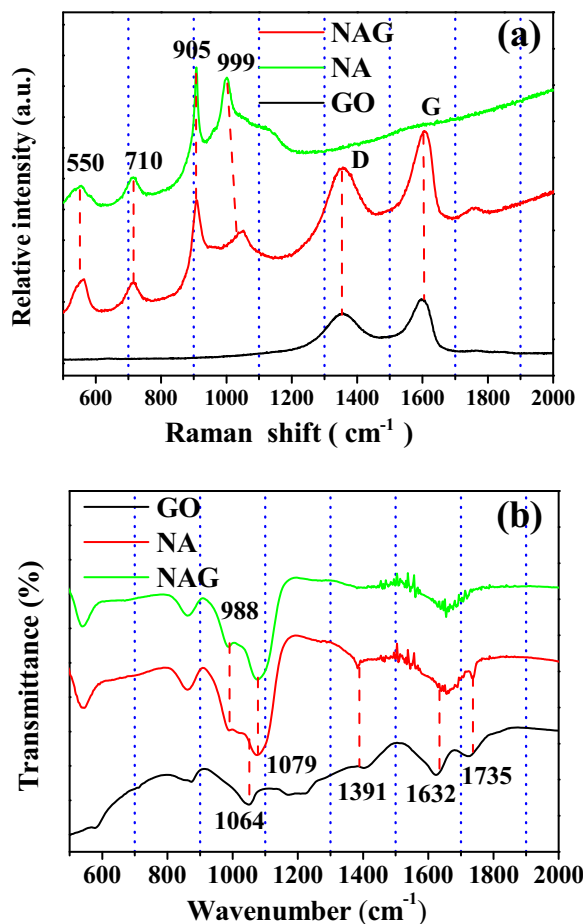


Fig. 5. Raman spectra (a) and FTIR spectra (b) of GO, the NA and NAG samples.

respectively [36]. However, the other two characteristic absorptions emerge at 1632 and 1735 cm^{-1} , which are related to the bending vibration of the hydroxyl group and the stretching vibration of carboxyl groups, respectively [36]. For Ag_3PO_4 , there are two typical absorption peaks at 988 and 1079 cm^{-1} , which correspond to the symmetric stretching vibration mode of the PO_4^{3-} group [37]. In the case of the Ag_3PO_4 -graphene composite (sample NAG), the typical absorption peaks of PO_4^{3-} group is also observed besides the four characteristic absorption peaks of GO. The above result suggests the existence of graphene in the composite sample and the integration of Ag_3PO_4 and graphene in the Ag_3PO_4 -graphene composite.

The X-ray photoelectron spectroscopy (XPS) was also carried out to further investigate the composition and the chemical status of the Ag_3PO_4 -graphene composite (sample NAG), and the results are shown in the Fig. 6. The high-resolution XPS spectrum (Fig. 6a) shows the binding energies of the Ag 3d_{5/2} and Ag 3d_{3/2} peaks at 368.0 and 374.0 eV , respectively, which are typical values for Ag^+ in Ag_3PO_4 [20]. Fig. 6b shows the high-resolution C 1s XPS spectra of the NAG sample in comparison to that of GO. As can be seen from this figure, the main C 1s peak at 284.8 eV for the both samples is observed, which is usually assigned to carbon and defect-containing sp^2 -hybridized carbon (C–C) atoms [25]. For GO, the C 1s peak at 287.1 eV is attributed to epoxy/hydroxyls (C–O), indicating the existence of oxygen-containing carbon in GO [25]. However, the peaks of the oxygen-containing carbon in GO at 287.1 eV become visibly weakened for the NAG sample. This result indicates that the introduced GO sheets in the synthesis system have been efficiently

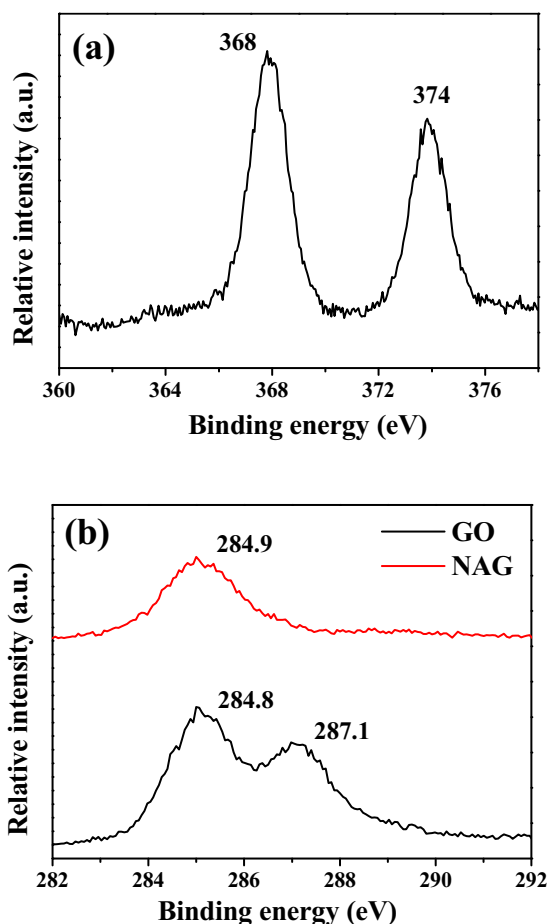


Fig. 6. High-resolution XPS spectra of Ag 3d (a) for the NAG sample and C 1s (b) for GO and the NAG sample.

transformed into reduced graphene oxide sheets during the synthesis process.

3.2. Photocatalytic activity and mechanism

The photocatalytic properties of the prepared NA, NAG, LA, LAG and N-TiO₂ samples were evaluated by monitoring the degradation of MB aqueous solution under visible light irradiation. Prior to irradiation, the mixed solution of MB and the photocatalyst was stirred in the dark for 30 min to establish the equilibrium adsorption state. It should be noted that the NAG sample exhibits the highest adsorption property in the all samples studied. This is due to the high specific surface area of Ag₃PO₄ nanoparticles and the presence of graphene in the NAG sample. The high adsorption performance of MB dyes on the NAG sample is beneficial to the photocatalytic degradation of MB dyes. Furthermore, control experiments indicated that MB dyes was not degraded under visible-light irradiation in the absence of the photocatalyst. Fig. 7a presents a comparison of the visible-light photocatalytic activity of the NA, NAG, LA, LAG and N-TiO₂ samples. As can be seen from this figure, all the Ag₃PO₄ samples exhibit super photocatalytic activity that is much better than the N-TiO₂ sample because of the strong visible-light absorption and the proper band edge potential of Ag₃PO₄. The further observation shows that the photocatalytic activity of the NA and LAG samples are higher than that of the LA sample. This is assigned to the high specific surface area for NA and the presence of graphene in LAG compared with LA. In particular, the NAG sample exhibits the highest photocatalytic activity among the all samples studied, which is mainly ascribed to the synergetic effects of two factors

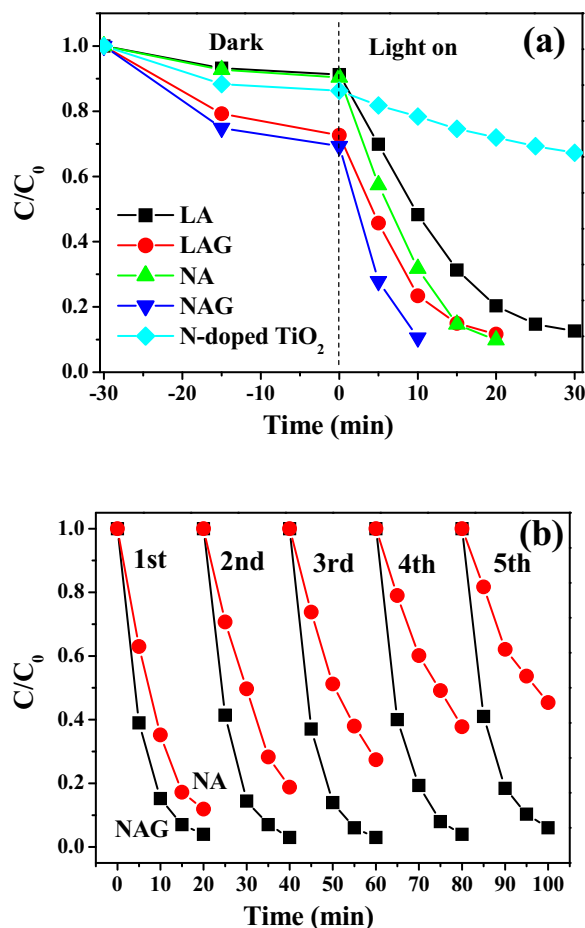


Fig. 7. (a) Comparison of the photocatalytic activity of the LA, LAG, NA and NAG samples, and N-doped TiO₂ for the photocatalytic degradation of MB aqueous solution under visible-light irradiation; (b) cyclic degradation curves for the NA and NAG samples.

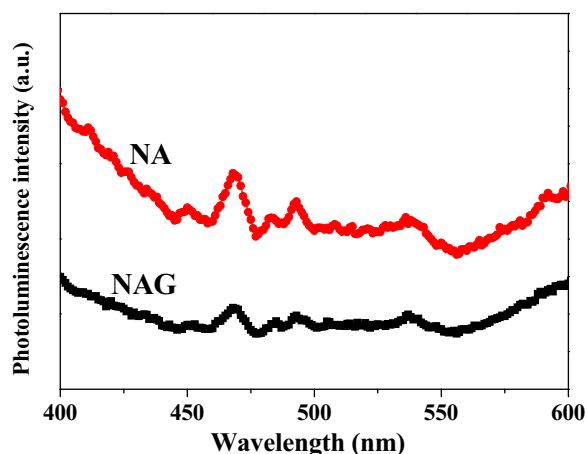


Fig. 8. Photoluminescence spectra of the NA and NAG samples.

including the large surface-to-volume ratio and the existence of graphene in the NAG sample. On the one hand, the relatively large surface-to-volume ratio of photocatalyst can provide more active sites for adsorption of MB dyes, and then resulting in the photocatalytic degradation process more efficiently. On the other hand, the photogenerated electrons of Ag₃PO₄ may transfer to graphene sheets in the composite due to the excellent electronic conductivity of graphene, leading to the separation of the photogenerated

electron–hole pairs. One direct evident is that the photoluminescence intensity of the NAG sample is much lower than that of the NA sample (see Fig. 8), indicating the Ag_3PO_4 –graphene composite has a smaller recombination and more efficient separation of the photogenerated electron–hole pairs. Therefore, it is not surprising that the efficiency of photocatalytic degradation of MB dyes over the NAG sample was much better.

To further investigate the photocatalytic stability of the NAG sample, recycle experiments of MB degradation on the NA and NAG samples were performed (see Fig. 7b). After five recycles for the degradation of MB, the photocatalytic activity of the NAG sample shows a little loss, indicating that the composite photocatalyst is relatively stable during the photocatalytic degradation of MB

dyes. However, for the NA sample (pure Ag_3PO_4), the photocatalytic efficiency decreased to 45% and changed its color from yellow to black after the fifth cycle. The results indicated that pure Ag_3PO_4 photocatalyst was unstable due to the formation of metallic Ag nanoparticles through the reduction of Ag_3PO_4 by photo-generated electrons under visible-light irradiation. This was also confirmed by TEM and the corresponding HRTEM images (see Fig. 9a and c) of the NA sample after 5 cycles, which clearly showed some small Ag nanoparticles on the surface of Ag_3PO_4 . On the contrary, metallic Ag nanoparticles were not observed for the NAG sample after five cycles (see Fig. 9b and d). Also, a relatively weak XRD diffraction peak at about 38° for the NA sample after five cycles can be indexed to the (1 1 1) lattice plane of metallic Ag (see Fig. 9e), but

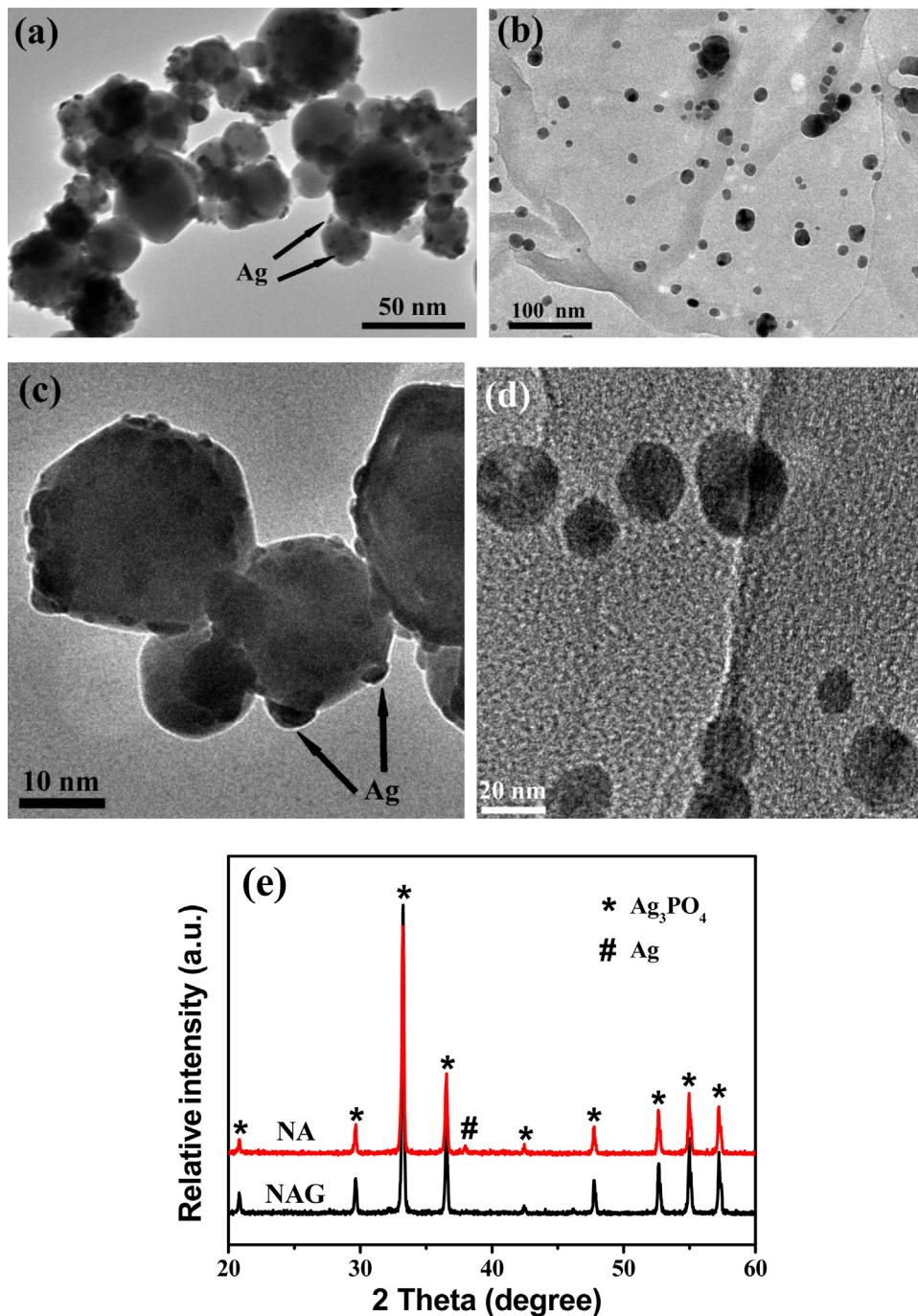


Fig. 9. TEM ((a) and (b)) and HRTEM ((c) and (d)) images, and XRD patterns (e) of the NA ((a) and (c)) and NAG ((b) and (d)) samples after 5 cycles.

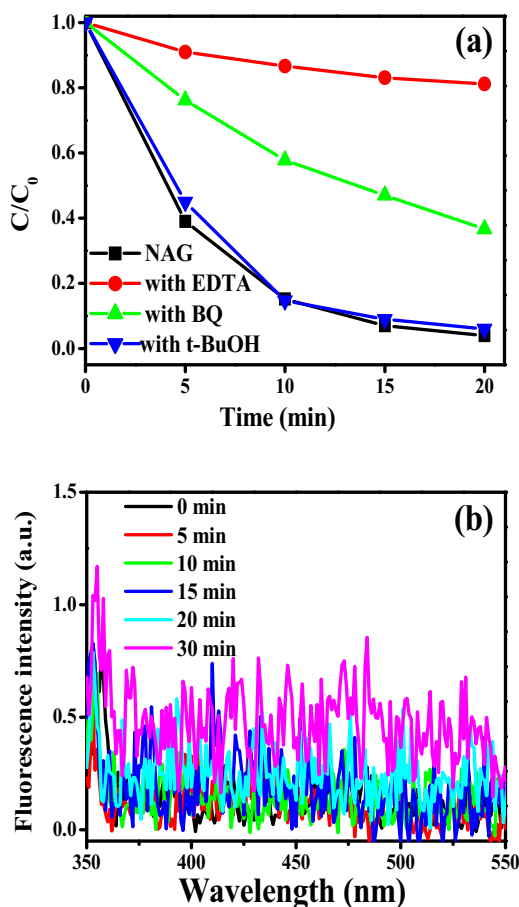


Fig. 10. (a) Photocatalytic activity of the NAG sample for the photocatalytic degradation of MB in the presence of different scavengers; (b) photoluminescence spectra in terephthalic acid solution of the NAG sample during visible-light illumination.

such a weak peak is not found in the XRD patterns of the NAG sample after five cycles. The above results indicate that the presence of graphene can prevent the formation of Ag nanoparticles on the surface of Ag_3PO_4 by receiving the photoinduced electrons on the graphene sheets, and then improve the photocatalytic stability of Ag_3PO_4 .

To elucidate the photocatalytic reaction mechanism, we attempted to examine the main reactive species including h^+ , $\bullet\text{O}_2^-$ and $\bullet\text{OH}$ involved in the photocatalytic process. In the experiments, disodium ethylenediaminetetraacetate (EDTA), benzoquinone (BQ), and *tert*-butanol (*t*-BuOH) acted as the scavengers for h^+ , $\bullet\text{O}_2^-$ and $\bullet\text{OH}$ were introduced into the photocatalytic reaction process, respectively. Fig. 10a shows a comparison of photocatalytic activity of the NAG sample for the degradation of MB in presence of different scavengers. It can be seen that the addition of 2 mM EDTA (holes scavenger) in the MB solution results in the fast deactivation of NAG for the degradation of MB. When 2 mM BQ ($\bullet\text{O}_2^-$ radical scavenger) was added, the efficiency of photocatalytic degradation was severely decreased. However, it was observed that the addition of 1 mL *t*-BuOH (hydroxyl radical scavenger) has little effect on the photocatalytic activity. The above results indicated that h^+ and $\bullet\text{O}_2^-$ were the main reactive oxidizing species in photocatalytic reaction process of NAG. While $\bullet\text{OH}$ may only play a less important role in the photocatalytic process. To further study $\bullet\text{OH}$ radicals involved in the photocatalytic process, $\bullet\text{OH}$ radicals were detected by a photoluminescence method using terephthalic acid as a probe molecule. The hydroxyl radical experiments (see Fig. 10b) show that no signal of $\bullet\text{OH}$ was observed for the irradiated NAG sample,

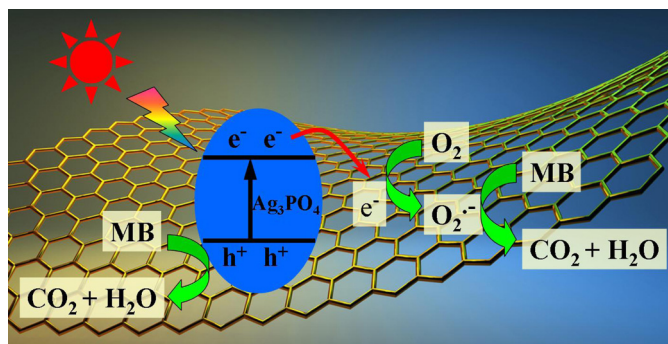
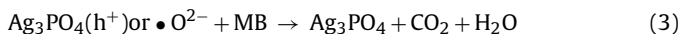
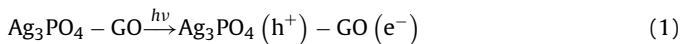


Fig. 11. Proposed photocatalytic mechanism for Ag_3PO_4 -graphene composite under visible-light illumination.

which indicates that no $\bullet\text{OH}$ were produced and $\bullet\text{OH}$ were not the main active oxygen species in photocatalytic reaction process. In fact, the valence band edge potential of Ag_3PO_4 and the $\text{OH}^-/\bullet\text{OH}$ couple potential are 2.8 and 2.7 eV *versus* SCE, respectively, and the photogenerated holes of Ag_3PO_4 cannot oxidize $\text{OH}^-/\text{H}_2\text{O}$ to form $\bullet\text{OH}$ due to their little difference of potentials [20].

Based on the above analysis, the possible photocatalytic mechanism of Ag_3PO_4 -graphene composite is proposed (Fig. 11). Under visible-light irradiation, electrons (e^-) are excited from the valence band (VB) of Ag_3PO_4 to the conduction band (CB), causing the generation of holes (h^+) in the VB. Normally, these photogenerated electrons and holes undergo recombination and a part of the charge carriers can migrate to the surface to participate in the photocatalytic reaction. However, when Ag_3PO_4 were dispersed on the surfaces of graphene sheets to form the composite, these photogenerated electrons on the CB of Ag_3PO_4 tend to transfer to graphene sheets, leading to the separation of hole-electron pairs. It has been reported that graphene has the fine electronic conductivity and excellent store electricity due to its specific π -conjugation structure, which could accelerate the transfer of photogenerated electrons into graphene sheets [38,39]. The transferred electrons can effectively suppress the charge recombination, reduce the formation of Ag nanoparticles and inhibit the photocorrosion of Ag_3PO_4 , which improves the photocatalytic efficiency and stability. Meanwhile, the photogenerated holes on the VB of Ag_3PO_4 can directly oxidize the MB dyes, while the electrons accumulating at graphene sheets could adsorb the ubiquitously present O_2 to form $\bullet\text{O}_2^-$, resulting in the degradation of MB dyes. The major reaction steps in the photocatalytic mechanism are summarized by the following equations:



4. Conclusions

In summary, a novel graphene-modified nanosized Ag_3PO_4 photocatalyst was prepared by *in situ* growth strategy in an organic solvent. It was shown that the as-prepared nanosized Ag_3PO_4 particles-graphene composite exhibits the enhanced visible-light photocatalytic activity and stability compared with bare nanosized Ag_3PO_4 particles and conventional large-sized Ag_3PO_4 particles-graphene composite. This arises from the positive synergistic effects between the nanosized Ag_3PO_4 particles and graphene sheets, which can provide a greater number of active adsorption sites, and suppress charge recombination and reduce the formation of Ag nanoparticles, and consequently improve the photocatalytic activity and stability. Considering the high photocatalytic efficiency

and stability, the novel nanosized Ag_3PO_4 particles–graphene composite photocatalyst is potentially applicable in environmental purification of organic pollutants.

Acknowledgements

The authors thank the National Natural Science Foundation of China (41271253), Specialized Research Fund for the Doctoral Program of Higher Education (20130146120040) and the Fundamental Research Funds for the Central Universities (Program numbers: 52902-0900206109 and 52204-12014) for financial support.

References

- [1] A.J. Bard, G.M. Whitesides, R.N. Zare, F.W. McLafferty, *Acc. Chem. Res.* 28 (1995) 91.
- [2] M.R. Hoffmann, S.T. Martin, W. Choi, D.W. Bahnemann, *Chem. Rev.* 95 (1995) 69–96.
- [3] X.B. Chen, S.H. Shen, L.J. Guo, S.S. Mao, *Chem. Rev.* 110 (2010) 6503–6570.
- [4] Q.J. Xiang, J.G. Yu, M. Jaroniec, *Chem. Soc. Rev.* 41 (2012) 782–796.
- [5] Q.J. Xiang, J.G. Yu, *J. Phys. Chem. Lett.* 4 (2013) 753–759.
- [6] Q.J. Xiang, J.G. Yu, M. Jaroniec, *J. Am. Chem. Soc.* 134 (2012) 6575–6578.
- [7] K. Lv, J.C. Hu, X.H. Li, M. Li, *J. Mol. Catal. A: Chem.* 356 (2012) 78–84.
- [8] P. Wang, J. Wang, T.S. Ming, X.F. Wang, H.G. Yu, J.G. Yu, Y.G. Wang, M. Lei, *ACS Appl. Mater. Interfaces* 5 (2013) 2924–2929.
- [9] H.G. Yu, L.L. Xu, P. Wang, X.F. Wang, J.G. Yu, *Appl. Catal., B: Environ.* 144 (2014) 75–82.
- [10] M. Ksibi, S. Rossignol, J.M. Tatibouët, C. Trapalis, *Mater. Lett.* 62 (2008) 4204–4206.
- [11] Q.J. Xiang, J.G. Yu, M. Jaroniec, *J. Phys. Chem. C* 115 (2011) 7355–7363.
- [12] Q.J. Xiang, B. Cheng, J.G. Yu, *Appl. Catal., B: Environ.* 138–139 (2013) 299–303.
- [13] Z.G. Yi, J.H. Ye, N. Kikugawa, T. Kako, S.X. Ouyang, H. Stuart-Williams, H. Yang, J.Y. Cao, W.J. Luo, Z.S. Li, Y. Liu, R.L. Withers, *Nat. Mater.* 9 (2010) 559–564.
- [14] Y.P. Bi, S.X. Ouyang, N. Umezawa, J.Y. Cao, J.H. Ye, *J. Am. Chem. Soc.* 133 (2011) 6490–6492.
- [15] Y.P. Bi, H.Y. Hu, S.X. Ouyang, Z.B. Jiao, G.X. Lu, J.H. Ye, *Chem. Eur. J.* 18 (2012) 14272–14275.
- [16] Y.P. Bi, H.Y. Hu, S.X. Ouyang, Z.B. Jiao, G.X. Lu, J.H. Ye, *J. Mater. Chem.* 22 (2012) 14847–14850.
- [17] C.T. Dinh, T.D. Nguyen, F. Kleitz, T.O. Do, *Chem. Commun.* 47 (2011) 7797–7799.
- [18] S.B. Rawal, S.D. Sung, W.I. Lee, *Catal. Commun.* 17 (2012) 131–135.
- [19] A. Khan, M. Qamar, M. Muneer, *Chem. Phys. Lett.* 519–520 (2012) 54–58.
- [20] W.G. Wang, B. Cheng, J.G. Yu, G. Liu, W.H. Fan, *Chem. Asian J.* 7 (2012) 1902–1908.
- [21] M.A. Gondal, X.F. Chang, W.E.I. Sha, Z.H. Yamani, Q. Zhou, *J. Colloid Interface Sci.* 392 (2013) 325–330.
- [22] L. Liu, J.C. Liu, D.D. Sun, *Catal. Sci. Technol.* 2 (2012) 2525–2532.
- [23] Y.P. Liu, L. Fang, H.D. Lu, Y.W. Li, C.Z. Hu, H.G. Yu, *Appl. Catal., B: Environ.* 115–116 (2012) 245–252.
- [24] X.F. Yang, H.Y. Cui, Y. Li, J.L. Qin, R.X. Zhang, H. Tang, *ACS Catal.* 3 (2013) 363–369.
- [25] Q.J. Xiang, J.G. Yu, M. Jaroniec, *Nanoscale* 3 (2011) 3670–3678.
- [26] Q. Li, B.D. Guo, J.G. Yu, J.R. Ran, B.H. Zhang, H.J. Yan, J.R. Gong, *J. Am. Chem. Soc.* 133 (2011) 10878–10884.
- [27] O. Akhavan, *ACS Nano* 4 (2010) 4174–4180.
- [28] G. Williams, P.V. Kamat, *Langmuir* 25 (2009) 13869–13873.
- [29] M.S. Zhu, P.L. Chen, M.H. Liu, *ACS Nano* 5 (2011) 4529–4536.
- [30] Y.X. Xu, H. Bai, G.W. Lu, C. Li, G.Q. Shi, *J. Am. Chem. Soc.* 130 (2008) 5856–5857.
- [31] Q.J. Xiang, J.G. Yu, W.G. Wang, M. Jaroniec, *Chem. Commun.* 47 (2011) 6906–6908.
- [32] K. Sing, D. Everett, R. Haul, L. Moscou, R. Pierotti, J. Rouquerol, T. Siemieniowska, *Pure Appl. Chem.* 57 (1985) 603–619.
- [33] Q.J. Xiang, J.G. Yu, B. Cheng, H.C. Ong, *Chem. Asian J.* 5 (2010) 1466–1474.
- [34] K. Ishibashi, A. Fujishima, T. Watanabe, K. Hashimoto, *J. Photochem. Photobiol., A: Chem.* 134 (2000) 139–142.
- [35] D. Lang, Q.J. Xiang, G.H. Qiu, X.H. Feng, F. Liu, *Dalton Trans.* 43 (2014) 7245–7253.
- [36] J. Li, S.B. Tang, L. Lu, H.C. Zeng, *J. Am. Chem. Soc.* 129 (2007) 9401–9409.
- [37] D. Boudlich, L. Bih, M.E.H. Archidi, M. Haddad, A. Yacoubi, A. Nadiri, B. Elouadi, *J. Am. Ceram. Soc.* 85 (2002) 623–630.
- [38] S. Stankovich, D.A. Dikin, G.H.B. Dommett, K.M. Kohlhaas, E.J. Zimney, E.A. Stach, R.D. Piner, S.T. Nguyen, R.S. Ruoff, *Nature* 442 (2006) 282–286.
- [39] S.M. Paek, E. Yoo, I. Honma, *Nano Lett.* 9 (2009) 72–75.